Parametrized process characterization with reduced resource requirements

Vicente Leyton-Ortega, Tyler Kharazi, and Raphael C. Pooser

Phys. Rev. A **105**, 052408 — Published 5 May 2022

DOI: 10.1103/PhysRevA.105.052408

Parameterized process characterization with reduced resource requirements*

Vicente Leyton-Ortega,† Tyler Kharazi, and Raphael C. Pooser
Computational Sciences and Engineering Division,
Oak Ridge National Laboratory, Oak Ridge, TN 37831, USA
(Dated: April 19, 2022)

Quantum Process Tomography (QPT) is a powerful tool to characterize quantum operations, but it requires considerable resources making it impractical for more than 2-qubit systems. This work proposes an alternative approach that requires significantly fewer resources for unitary process characterization with a built-in method for state preparation and measurement (SPAM) error mitigation. By measuring the quantum process as rotated through the X and Y axes on the Bloch Sphere, we can acquire enough information to reconstruct the quantum process matrix χ and measure its fidelity. We test the algorithm's performance against standard QPT using simulated and physical experiments on several IBM quantum processors and compare the resulting process matrices. We demonstrate in numerical experiments that the method can improve gate fidelity via a noise reduction in the imaginary part of the process matrix, along with a stark decrease in the number of experiments needed to perform the characterization.

I. INTRODUCTION

Modern quantum computers are marred by noise that limits their computational reach. The sources of this noise are myriad, including initial state preparation errors, noise introduced during the computation via decoherence and gate noise, and imprecise state readout at measurement [1]. There has been extensive work to improve quantum processor units (QPUs) at the hardware level with methods that are generally not accessible at the end-user level. Given the current proliferation of noisy intermediate-scale quantum (NISQ) resources, we seek strategies that end-users can use to calibrate a set of qubits on physical, could-based, QPUs in a cost-effective (less resource-intensive) manner. Furthermore, these algorithms serve to isolate and characterize noise, a critical component in benchmarking performance on experimental devicues. [2].

One such characterization method, quantum tomography, provides a set of tools to characterize the behavior of quantum dynamical processes through a series of measurements spanning a complete basis, typically the Pauli basis. Standard quantum process tomography (QPT) reconstructs the underlying quantum process $\mathcal{E}$ by performing state tomography on a set of identical quantum states after applying certain quantum operations, i.e., a quantum circuit [3–5]. Through this tomographic reconstruction in state space, one can infer the region where each generated state lies by applying maximum likelihood estimation [6], Bayesian credibility [7, 8], or confidence regions [9–11].

Process tomography is also a key component in noise characterization and noise mitigation for quantum algorithms [12]. Through a large number of circuit evaluations or shots, one can deploy statistical and numerical methods to infer the underlying process matrix representation of $\mathcal{E}$ [13–15]. However, the resource requirements inhibit the scalability of QPT-based methods on NISQ hardware. For an informationally complete determination of an n-qubit quantum process, one needs to prepare $4^n \times 3^n$ independent circuit executions to completely specify a quantum process(see Appendix A for more details). This resource overhead makes QPT impractical for characterizing processes involving more than a few qubits. For example, the complete characterization of a 3-qubit quantum process requires $12^3 = 1728$ independent experiments, with each experiment repeated many times to gather sufficient statistics. On the publicly available IBM QPUs, i.e., `IBMQ Bogota`, a user can send at most 900 independent experiments, falling far short of the 1728 required to characterize a 3-qubit process fully. One may send the complete set of experiments in two separate batches of circuits, but this leaves open the possibility that the device may have changed significantly between experimental runs. Without dedicated access to a QPU, process tomography is practically challenging for $n > 3$ qubit systems. There has been promising improvements to ameliorate this unfavorable scaling via ancilla-[16–20] and error-correction-based[21–24] QPT schemes. These methods require sophisticated state and measurement preparations. Bayesian compressed sensing methods have also been shown to reduce the number of experiments if some prior information about the process is known[25, 26]. However, the success of compressed sensing depends on the accuracy of the rank knowledge given for the quantum process[27, 28]. Another way to reduce the resource requirements consists of a partial characterization, like the randomized benchmarking used to

† Corresponding author: leytonorteva@ornl.gov

compute gate fidelities on superconducting QPUs [29–31]. In summary, these methods assume a specific structure: low-rank restrictions [28], two-qubit processes [32], and a unitary structure that only requires measurements of the diagonal elements of the rotated process matrix.

Progresses in QPT techniques with fewer restrictions on the quantum process to reduce the number of experiment resources have been developed recently, where one can characterize unitary quantum processes with *no further prior* knowledge with a reduced number of measurements. Baldwin *et al.* study the problem of QPT under the assumption that the target quantum process is unitary (or close to) by discriminating the target process from any other CTPT process (a.k.a. BKD scheme). An improved compressed-sensing protocol was introduced by Ahn *et al.* [33, 34], introducing an adaptive compressive tomography scheme (ACT) inspired by the traditional compressed-sensing protocol in signal recovery. This adaptive technique does not rely on any prior information about the quantum state apart from its dimension. Recently, ACT has been extended for quantum process characterization (ACTQPT) [35] and tested in numerical and physical experiments. The ACTQPT can characterize any quantum process with fewer measurement resources than the standard QPT. This quantum process characterization has been improved by implementing an informational completeness certification [36] that certifies the reconstruction uniqueness of the acquired data in the characterization. In those schemes, the number of required experiments, $O(4^n)$, for a complete characterization is exponentially smaller than the number required in the standard QPT. Another common characteristic is the idealized measurement and state preparation, where the measurement process does not record assignation errors, and the preparation of quantum states for the characterization is not subject to coherent and incoherent errors.

In synthesis, QPT techniques assume an idealized limit, yet they are susceptible to state preparation and measurement errors (SPAM) [2, 14]. This assumption can lead to underestimating process fidelity by rolling SPAM errors into the same process as the gates one is trying to characterize. Here, we reduce the complexity of QPT only with the unitary-process assumption while still offering an exponential improvement in resource cost over standard QPT by assuming a straightforward noise model consisting of bit-flip assignment readout error and an over-rotation error (see Fig. 2). Characterization uses a series of rotations and measurements tailored to limited access quantum chips such as cloud-based IBM quantum devices, which we dub parametrized process characterization (PPC). We further provide a method to unravel SPAM errors from process characterization by fitting the projective measurement of key quantum states generated by the quantum process to a statistical model influenced by SPAM-type errors. The resulting fit parameters then allow us to reconstruct the underlying quantum process.

II. METHODS

To illustrate the general idea of PPC, we first give a one-qubit example that can be extended to a more general case. We wish to characterize some quantum process $\mathcal{U} : \rho \to U\rho U^\dagger$, with ρ and U as a one-qubit quantum state and unitary operator, respectively. Without loss of generality, we shall consider the rotation $Y_\theta = \exp[-i\theta\sigma_y/2]$ and assume that rotation is a noiseless unitary operation in the experimental setup. The projective measurement, along the z-axis in the Bloch sphere, of the state $Y_\theta U|s\rangle$, for $|s\rangle \in \{|0\rangle, |1\rangle\}$, reads

$$P_s^{\mathcal{U}}(\theta) = \begin{pmatrix} s_{\theta/2}^2 + |U_{s,0}|^2 c_\theta - (U_{s,0}U_{s,1}^* + U_{s,1}U_{s,0}^*)s_\theta \\ s_{\theta/2}^2 + |U_{s,1}|^2 c_\theta + (U_{s,0}U_{s,1}^* + U_{s,1}U_{s,0}^*)s_\theta \end{pmatrix}, \tag{1}$$

with $U_{kl} = \langle l|U|k\rangle$, $c_\theta = \cos\theta$, and $s_\theta = \sin\theta$.

As a physical interpretation, we consider the rotation around the y-axis in the Bloch sphere of an arbitrary quantum state $|\varphi\rangle$. The projection on the z-axis of the rotated state corresponds to the mean value $\langle\sigma_z\rangle_{\theta_s} = \langle\sigma_z\rangle_\varphi c_{\theta_s} + \langle\sigma_x\rangle_\varphi s_{\theta_s}$, this mean value is an experimentally accessible quantity for every value of θ_s, and therefore, it defines a way to determine by a fitting procedure the observables $\langle\sigma_z\rangle_\varphi$ and $\langle\sigma_x\rangle_\varphi$ that constitutes the characterization of the state $|\varphi\rangle$.

To account for readout error, we introduce a classical assignment error modeled by the transition matrix:

$$T = \begin{pmatrix} t_{00} & 1 - t_{11} \\ 1 - t_{00} & t_{11} \end{pmatrix}, \tag{2}$$

with t_{00} and t_{11} as the probabilities of measuring correctly the states $|0\rangle$ and $|1\rangle$, respectively. T is obtained experimentally via calibration measurements. This matrix represents a binary asymmetric channel, i.e., $t_{00} \neq t_{11}$, that maps the original probability distribution to the experimental observation $Q_s^{\mathcal{U}}(\theta) = T \cdot P_s^{\mathcal{U}}(\theta)$, which can be rewritten as:

$$Q_s^{\mathcal{U}}(\theta) = \begin{pmatrix} 1 - t_{11} \\ 1 - t_{00} \end{pmatrix} + |T| P_s^{\mathcal{U}}(\theta - \theta_0). \tag{3}$$

This equation establishes a way to determine the quantum process by fitting $U_{s,0}$ and $U_{s,1}$ with the experimental data T and $Q_s^{\mathcal{U}}(\theta)$. Notably, with the assumption that a transition matrix can describe readout errors and those errors occur only along the direction of rotation, a single parameter in Eq. 3 can be used to fit the data. Here θ_0 is an initial phase representing either a state preparation error or a compilation error in the rotation operator Y_θ. In summary, we evaluate the action of the unitary operator U on a set of rotated states $Y_\theta|0\rangle$, and by fitting the model for the measurement output $T \cdot P_s^{\mathcal{U}}(\theta)$ to the experimental output $Q_s^{\mathcal{U}}(\theta)$ in (see Eq. 3), we can estimate the components for U on the computational basis.

This procedure can be extended to an n-qubit system, considering Y_θ^s as the main rotation; the superscript s

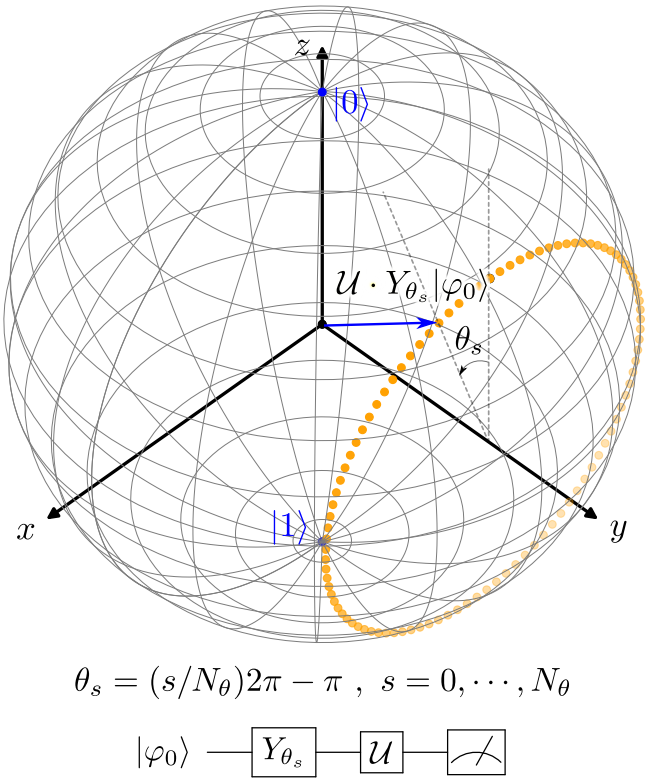

FIG. 1. Diagrammatic sketch of PPC in the Bloch sphere for one-qubit systems. With the information obtained from rotation on the states $\mathcal{U}|0\rangle$ and $\mathcal{U}|1\rangle$ we get information about the quantum process represented by $\mathcal{U}$. The dotted lines represent the rotations of the states $\mathcal{U}|0\rangle$ and $\mathcal{U}|1\rangle$ around the y-axis. In order to clarify this procedure, inset displays the mean value $\langle\sigma_z\rangle_{\theta_s}$ (experiment's output) as a function of θ_s. There, the behavior of $\langle\sigma_z\rangle_{\theta_s}$ for different values of θ_s gives information about the observables $\langle\sigma_z\rangle_\varphi$ and $\langle\sigma_x\rangle_\varphi$ that conform the tomography information of the state $|\varphi\rangle = \mathcal{U}|\varphi_0\rangle$.

stands for the physical qubit where the rotation is applied. As before, it is enough to consider a subset of the n-qubit computational basis where the s-th qubit is in the ground state, i.e., the set $\{|\varphi_{k,s}\rangle = |k_0, \cdots, k_{2^n}\rangle \in \{|0\rangle, |1\rangle\}^n : k_s = 0\}$, and determine the action of the unitary operator U on different rotations applied on this set,

$$|\psi_{k,s}(\theta)\rangle = U \cdot Y_\theta^s |\varphi_{k,s}\rangle \tag{4}$$

for different values of θ in $[-\pi, \pi]$. The projective measurement from these states, $T \cdot P^{\mathcal{U}}_{k,s}(\theta)$, can be seen as a function of θ with parameters given by the components of U, i.e., a function $F_{k,s}(\theta; U_{00}, \cdots, U_{(2^n,2^n)})$. Thus, the fit parameters of this function to the experimental measurement data give the estimate for U. Before applying the algorithm, we use a calibration procedure to determine the transition matrix T and the phase correction θ_0 that uses a similar angular sweep (see Section V).

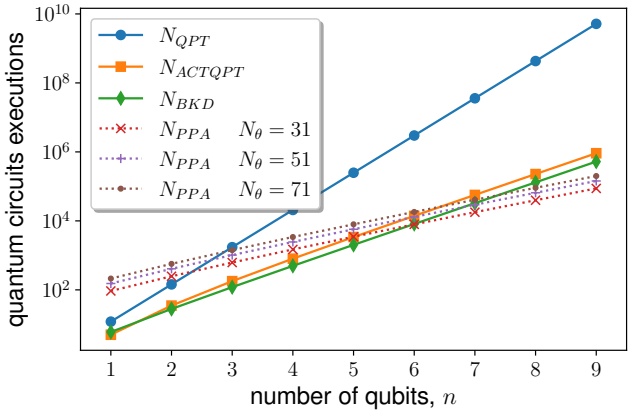

FIG. 2. *Number of quantum circuit executions for quantum process characterization:* in this figure, we compare the resources used by different QPT techniques against the resources used by PPC. For different numbers of rotations ($N_\theta = 31, 51$,and 71 lines), standard QPT surpasses PPC in the number of resources required for its execution for $n > 2$, and state-of-the-art techniques like ACTQPT and BKD surpasses PPC for $n > 6$.

III. SINGLE QUBIT QUANTUM PROCESS CHARACTERIZATION

For an n-qubit quantum process characterization $\mathcal{U}$, it is necessary to execute $N_{PPC} = 2^{n-1}(n+2)N_\theta$ quantum circuits with N_θ as the number of rotations the interval $[-\pi, \pi]$ is divided into; $2^n N_\theta$ quantum circuits for calibration; and $2^{n-1} n N_\theta$ quantum circuits to obtain data for fitting an estimate of U. Both the calibration and the estimation quality depends on N_θ -a large enough value ensures slight deviations ($\sigma \sim N_\theta^{-1/2}$) of the model from the experimental data. Note that N_θ does not depend on the number of qubits. Since QPT scales differently with the number of qubits, $N_{QPT} = 12^n$, PPC with a moderate number of angles becomes a favorable method in cases where $n > 2$, since $\log(N_{QPT}/N_{PPC}) \sim (n-1)\log 6 - \log(N_\theta/2)$. Concerning state-of-the-art schemes, like ACTQPT and BKD, the PPC shows a reduction in the measurement resources for $n > 6$. PPC is still being a good method when considering the SPAM mitigation embedded in the protocol. Figure 2 shows resource scaling for each protocol.

We performed simulations and on-hardware experiments for one and two-qubit systems using native gates as the target operations to characterize. See appendix C for the quantum hardware specifications. For these experiments, we set $N_\theta = 51$ rotations and $N = 5000$ experimental repetitions of PPC circuits and employ the Python Symfit [37] library to fit the model to the experimental data. Symfit is a Python module that uses symbolic methods to determine the Jacobian in the fitting process analytically. We test our procedure characterizing the X- and H-gate for one-qubit systems and

the CX-gate for two-qubit systems applied on different plaquettes on several IBM QPUs. We use Y_θ for the calibration and characterization since this rotation has lower fidelity than X_θ (see appendix B), and thus constitutes a good benchmark for the method. For the QPT experiments, we use the tomography module of Qiskit Ignis [38].

A common way to describe the quantum process $\mathcal{U}$ is through the process matrix χ defined as

$$\mathcal{U}(\rho) = \sum_{kl} \chi_{kl} P_k \rho P_l, \tag{5}$$

with ρ as a one qubit state, and $P_k \in \{\mathbb{I}, \sigma_x, \sigma_y, \sigma_z\}$ (Pauli basis). It is simple to find the process matrix χ, we need to find the representation of U in the Pauli basis and compare $U\rho_0 U^\dagger$ with Eq. (5), which gives $\chi_{kl} = u_k u_l^*$ with $u_k = \mathrm{tr}\{\mathcal{U}P_k\}/2$.

When comparing QPT and PPC-generated process matrices, we observe qualitatively similar results for the real part, χ_{re}, while observing differences in the imaginary part, χ_{im}. In Figures 3 and 4, we present the heat plots of the process matrix from the numerical and *on-hardware* experiments comparing both methods using the gates H and CX as targets, respectively. We further observe that the χ_{im}^{PPC} differs from χ_{im}^{QPT}, even in the noiseless numerical experiments. The imaginary part, which gives information about the quantum error [14], in both procedures is slightly different, owing to the assignment error mitigation implemented in PPC. This isolation of SPAM errors is impossible to do under standard QPT. A common way to compare the empirical and the expected operation is through the process fidelity $F_\chi = \mathrm{tr}[\chi\chi_0]/4^n$, with χ_0 as the noiseless process matrix. In table I, we show the process fidelity values for every experiment. The PPC results show closer values to 1 than the QPT results in the numerical experiments, where we used a noiseless simulator as the initial test of the method. In the physical experiments, we still observe that χ_{PPC} has a minor contribution from the imaginary part than the result from χ_{QPT}. The numerical results for χ_{im}^{PPC} and χ_{im}^{QPT} are irrelevant since the statistical error $N^{-1/2}/2 \sim 7 \times 10^{-3}$[39] in the projective measurement. For the physical experiment, we observed similar values for one- and two-qubit in the standard deviation ($\sigma_{PPC} \sim 2 \times 10^{-3}$ and $\sigma_{QPT} \sim 6 \times 10^{-3}$) after bootstrapping results from 21 experiments using each method in 10^4 resamples. These deviations determine what values are statistically relevant in the experiment. Therefore, the results for one-qubit experiments are closer to an ideal behavior than the results from two-qubit gates. Additionally, we determine the difference between the process matrices χ^{PPC} and χ^{QPT} applying the distance $d_\infty(\cdot,\cdot)$.

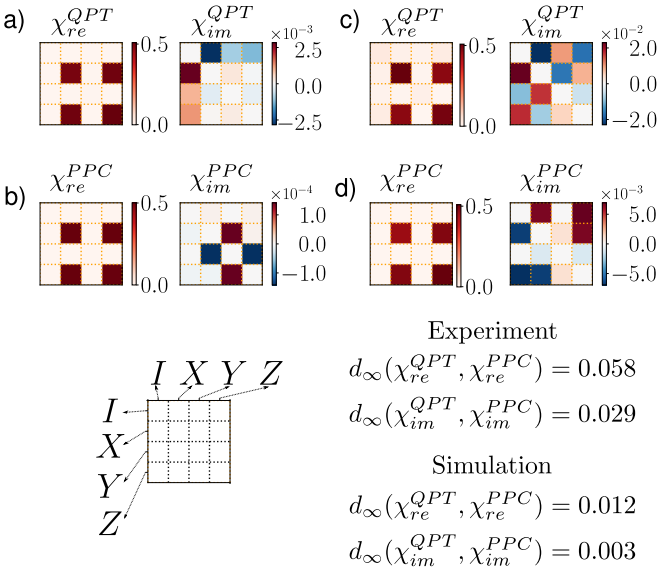

FIG. 3. Comparison between tomography results for the one-qubit system. We present the χ-matrix representation in the Pauli matrices for the Hadamard gate H using QPT and PPC. In a) and b), we depict the χ-matrix using QPT and PPC, respectively, by running the experiment in a noiseless simulator. In c) and d), we show the resulting χ matrices, by QPT and PPC, respectively, by running the experiment on the 0th qubit on the IBMQ-Bogota backend. In both cases, we considered $N = 5000$ shots and least square estimation for QPT, and $N = 5000$ shots and $N_\theta = 51$ for PPC. There is a good agreement in the χ-matrix's real part, but a difference in the imaginary part, even when using the noiseless simulator. In the noiseless simulator, the imaginary part is statistically irrelevant since the statistical error is in the order of $N^{-1/2}/2 \sim 7 \times 10^{-3}$[39]. On the other hand, in the QPT experiments, the imaginary part is statistically relevant due to SPAM errors. At the bottom, we present the $d_\infty(\cdot)$ distance between the resulting process matrices.

A. density matrix representation of the one-qubit characterization

For the sake of clearness, we describe the scheme for the one-qubit quantum process characterization in the density matrix representation. To this end, we consider the super-operator notation, in which the density operator ρ is written as a super-ket $|\rho\rangle\rangle$. In this case, consider the initial state $|\rho_0\rangle\rangle = (1,0,0,0)^{\mathrm{T}}$.

IV. MULTI-QUBIT QUANTUM PROCESS CHARACTERIZATION

Consider the action of a n-qubit quantum operator $\mathcal{U}$ on the state

$$\begin{aligned} |\psi_{k,s}(\theta)\rangle\rangle &= Y_\theta^s |k_0, \cdots, k_{s-1}, 0, k_{s+1}, \cdots, k_n\rangle\rangle \\ &= Y_\theta^s |k, 0_s\rangle\rangle. \end{aligned} \tag{6}$$

TABLE I. Process fidelity F_χ of local and non-local gates.

configuration	gate	F_χ PPC	F_χ QPT
Numerical		1.0	0.99
IBMQ-Bogota, qubit 0		0.99	0.92
IBMQ-Bogota, qubit 2		0.99	0.95
IBMQ-Santiago, qubit 1	X	0.99	0.97
IBMQ-Santiago, qubit 3		0.99	0.99
IBMQ-Quito, qubit 0		0.92	0.93
IBMQ-Quito, qubit 1		0.99	0.99
IBMQ-Boeblingen, qubit 0		0.99	0.96
IBMQ-Boeblingen, qubit 4		0.99	0.92
Numerical		1.0	0.99
IBMQ-Bogota, qubit 0		0.96	0.90
IBMQ-Bogota, qubit 2		0.99	0.95
IBMQ-Santiago, qubit 1	H	0.99	0.97
IBMQ-Santiago, qubit 3		0.99	0.99
IBMQ-Quito, qubit 0		0.93	0.94
IBMQ-Quito, qubit 1		0.99	0.99
IBMQ-Boeblingen, qubit 0		0.99	0.95
IBMQ-Boeblingen, qubit 4		0.96	0.90
Numerical		1.0	0.98
IBMQ-Bogota, qubits [1,2]		0.97	0.75
IBMQ-Bogota, qubits [0,1]	CX	0.96	0.73
IBMQ-manhattan, qubits [0,1]		0.99	0.88
IBMQ-manhattan, qubits [11,17]		0.99	0.98
IBMQ-Boeblingen, qubit 0		0.99	0.86
IBMQ-Boeblingen, qubit 4		0.99	0.81

V. CALIBRATION

We assume the assignment error effects are represented by a transition matrix $T_{kl} = P(l|k)$, where $P(l|k)$ is the conditional probability of observing $|j\rangle$ when the system has been prepared in the state $|i\rangle$. This is typically determined by measuring the number of outcomes 'j', c_j, of N identically-prepared states of $|i\rangle$; $T_{ij} = c_j/N$. However, this procedure is limited in its explanatory power, as we cannot determine which part of the readout error comes from the state preparation. Additionally, this method scales exponentially with the number of qubits considered since we must evaluate the conditional probabilities for all 2^n states of the system. We follow a modified calibration routine that tracks assignment error as a function of the rotation about the y-axis to discriminate the assignment error from every possible state preparation error in each experiment.

We rotate the states $|0, k_0, \cdots, k_{n-1}\rangle$ around the y-axis of the first qubit, for $k \in \{0,1\}^{n-1}$, yielding the output $c_{\theta/2}|0, k_0, \cdots, k_{n-1}\rangle + s_{\theta/2}|1, k_0, \cdots, k_{n-1}\rangle$. Thus, the expected probability distribution will have two components, $c^2_{\theta/2}$ and $s^2_{\theta/2}$, for instance

$$
\begin{aligned}
P_{k=0\cdots0}(\theta) &= (c^2_{\theta/2}, \underbrace{0, \cdots, 0}_{2^{n-1}-1}, s^2_{\theta/2}, 0, \cdots, 0)^T, \\
P_{k=10\cdots0}(\theta) &= (0, c^2_{\theta/2}, \underbrace{0, \cdots, 0}_{2^{n-1}-2}, 0, s^2_{\theta/2}, 0, \cdots, 0)^T, \\
&\vdots \\
P_{k=0\cdots01}(\theta) &= (\underbrace{0, \cdots, 0}_{2^{n-1}-1}, c^2_{\theta/2}, 0, \cdots, 0, s^2_{\theta/2})^T.
\end{aligned}
\tag{11}
$$

Under the bit-flip noise model, an empirical probability distribution $Q_k(\theta)$ is related to $P_k(\theta)$ by $Q_k(\theta) = T \cdot P_k(\theta)$, with

$$
T = \begin{pmatrix} t_{00} & \cdots & t_{0,2^n} \\ \vdots & \ddots & \vdots \\ t_{2^n,0} & \cdots & t_{2^n,2^n} \end{pmatrix} . \tag{12}
$$

Taking into account the structure of $P_k(\theta)$, we can determine two columns of T per state $Y_\theta|0, k_0, \cdots, k_{n-1}\rangle$. Above, we used a short notation to identify where the rotation is being applied, in this case on the ground state of the s-th qubit while the rest are at $|k_0, \cdots, k_{s-1}, k_{s+1}, \cdots, k_n\rangle$. The probability distribution for $\mathcal{U}|\psi_{k,s}(\theta)\rangle$ reads as

$$
P^{\mathcal{U}}_{k,s}(\theta) = \frac{1}{2}\left(A_{k,s} + B_{k,s}\, c_\theta + C_{k,s}\, s_\theta\right), \tag{7}
$$

where $A_{k,s}$, $B_{k,s}$, and $C_{k,s}$ are vectors in $\mathbb{R}^{2^n}$, with components

$$
[A_{k,s}]_j = |\langle j|\mathcal{U}|k, 0_s\rangle|^2 + |\langle j|\mathcal{U}|k, 1_s\rangle|^2 , \tag{8}
$$

$$
[B_{k,s}]_j = |\langle j|\mathcal{U}|k, 0_s\rangle|^2 - |\langle j|\mathcal{U}|k, 1_s\rangle|^2 , \tag{9}
$$

$$
\begin{aligned}
[C_{k,s}]_j = \langle j|\mathcal{U}|k, 0_s\rangle\langle j|\mathcal{U}|k, 1_s\rangle^* + \\
\langle j|\mathcal{U}|k, 0_s\rangle^*\langle j|\mathcal{U}|k, 1_s\rangle,\ j \in \{0,1\}^n .
\end{aligned}
\tag{10}
$$

By measuring N systems identically prepared in the state $\mathcal{U}|\psi_{k,s}(\theta)\rangle$ for every θ in $\mathcal{S}_{N_\theta} = \{(j/N_\theta - 1)\pi : j \in \mathbb{N}, 0 \le j \le N_\theta\}$; we estimate the probability distributions $Q^j_{k,s} = (\mathrm{C}^{k,j}_0/N, \cdots, \mathrm{C}^{k,j}_{2^n}/N)$ for $j = 0, \cdots, N_\theta$, with $\mathrm{C}^{k,j}_m$ as the number of outcomes 'm' $\in \{0,1\}^n$ for the j-th angle. The original distributions $P^j_{k,s}$, after mitigating the assignment error (see next section for details), are obtained by minimizing the functions $f_j(P) = ||Q^j_{k,s} - T \cdot P||_F$, where $||\cdot||_F$ is the Frobenius norm. With that information, i.e. $\{P^0_{k,s}, \cdots, P^{N_\theta}_{k,s}\}$ and the model (7), we can compute the matrix elements for $\mathcal{U}$. Therefore, we can determine the process matrix χ.

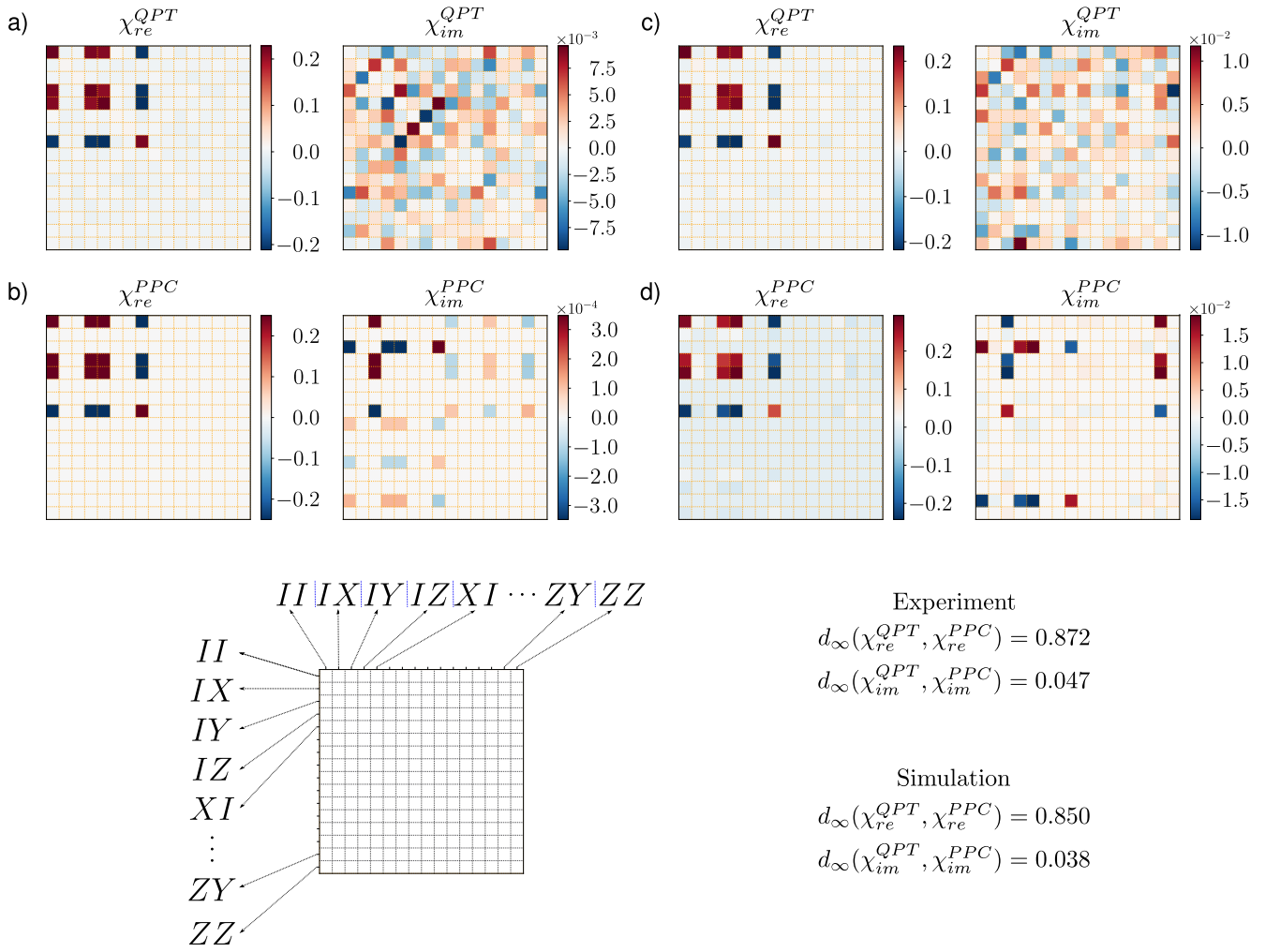

FIG. 4. *χ-matrix for the CX-gate:* Here we depict the χ-matrix representation in Pauli matrices of the CNOT-gate, obtained by the QPT and PPC methods. In a) and b) we used a noiseless simulator to run QPT and PPC, respectively. In c) and d), we used the qubits 0 and 1 on IBMQ-Bogota backend to run QPT and PPC respectively. In the experiments we used $N = 5000$ shots and least squared estimation for the QPT configuration, and $N = 5000$ shots and $N_\theta = 51$ for the PPC configuration. We obtained similar results to the one-qubit case, there is good agreement with the real part, but a slight difference in the imaginary ones. Again, part of the imaginary values stem from an inherent error introduced by the estimation procedure in the QPT method. In this case, the imaginary part produced by PPC and QPT in the numerical experiments are still statistical no relevant since we can consider the same level of statistical error used in the one-qubit case [39], i.e. $\sim 7 \times 10^{-3}$. For the physical experiments, the imaginary part overpass the standard deviations ($\sigma_{PPA} \sim 2 \times 10^{-3}$ and $\sigma_{QPT} \sim 6 \times 10^{-3}$) reveling imperfections in the quantum gate. In this case, the distance $d_\infty(\cdot, \cdot)$ in the simulation is similar with the experimental result.

We measure the states $Y_{\theta_j}|0, k_0, \cdots, k_{n-1}\rangle$, $\theta_j \in \mathcal{S}_\theta$, and estimate the probability distribution by the sampling distribution of the outcomes, i.e. we obtain the quantities $Q_k^j = (\mathrm{C}_0^{k,j}/N, \cdots, \mathrm{C}_{2^n}^{k,j}/N)^T$. We fit the acquired data with the model $T \cdot P_k(\theta - \theta_0)$. In the model, we have considered an initial phase θ_0 to describe preparation error.

A. Two-qubit transition matrix and initial preparation

For the two-qubit system, we can consider the following model for the expected distributions of the states $Y_\theta^0|00\rangle$ and $Y_\theta^0|01\rangle$,

$$P_0(\theta) = (c_{\theta/2}^2, 0, s_{\theta/2}^2, 0)^T,$$
$$P_1(\theta) = (0, c_{\theta/2}^2, 0, s_{\theta/2}^2)^T, \tag{13}$$

and the emperical distributions $Q_k(\theta) = T \cdot P_k(\theta)$,

$$Q_0(\theta) = \begin{pmatrix} t_{00} \\ t_{10} \\ t_{20} \\ t_{30} \end{pmatrix} c^2_{\theta/2} + \begin{pmatrix} t_{02} \\ t_{12} \\ t_{22} \\ t_{32} \end{pmatrix} s^2_{\theta/2},$$
$$Q_1(\theta) = \begin{pmatrix} t_{01} \\ t_{11} \\ t_{21} \\ t_{31} \end{pmatrix} c^2_{\theta/2} + \begin{pmatrix} t_{03} \\ t_{13} \\ t_{23} \\ t_{33} \end{pmatrix} s^2_{\theta/2}. \tag{14}$$

Now, we execute the quantum circuits

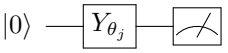

for $k = 0$, (15)

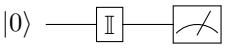

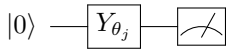

for $k = 1$, (16)

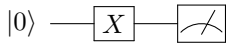

and for $\theta_j \in \mathcal{S}_\theta$. We determine the transition matrix elements t_{ij} by fitting the model (14) to the acquired data $Q^j_k = (\mathrm{C}^{k,j}_{00}/N, \mathrm{C}^{k,j}_{01}/N, \mathrm{C}^{k,j}_{10}/N, \mathrm{C}^{k,j}_{11}/N)^T$ from the above quantum circuit executions.

VI. DISCUSSION

To summarize, we introduced an alternative method to characterize a unitary quantum process based on a rotational sweeping procedure without prior information about the process. Instead of using a complete set of measurement operators, we measure the unknown quantum state rotated around different angles. Additionally, we proposed a pre-characterization process to define the assignment errors enclosed in the transition matrix and then mitigated those effects in the quantum process characterization. In the scheme presented here, we perform $2^{n-1}(n+2)N_\theta$ experiments to characterize an n-qubit process, in which the number of angles N_θ does not scale with the number of qubits. Therefore, we can fix this parameter to get enough data to fit the model with minor deviations. We considered $N_\theta = 51$ for a suitable fitting with relatively slight deviations ($\sim 10^{-4}$) from ideal behavior; this value can be used for any n-qubit system. Additionally, QPT is affected by errors in preparing the initial states and tomography measurements. By contrast, in our method, we control the initial preparation error by considering an initial phase in the model and the readout error by mitigating the assignment error.

The PPC algorithm is affected by the fitting error that depends on the number of rotational divisions, N_θ. This procedure assumes a high-fidelity rotation and trusted quantum states $|0\rangle$ and $|1\rangle$ in the same way that QPT relies on high-fidelity measurement. One way to mitigate a possible imperfection in the rotation process is by using a different compilation for the rotations Y_θ and X_θ. For instance, we can use the compilation procedure introduced in [40]; a decomposition based on rotations X_θ. The alternative decomposition brings a shorter pulse structure and commensurately higher fidelity.

To validate the performance of the PPC procedure, we compared the process matrix obtained by our approach with the outcome from the QPT. We compared the process fidelity F_χ of the results, from PPC and QPT, of different one- and two-qubits gates *on-hardware* and *in-silico*. As expected, we found minor differences between $\mathrm{Re}\{\chi_{PPC}\}$ and $\mathrm{Re}\{\chi_{QPT}\}$; there was, however, a remarkable difference in their imaginary parts, even in the numerical experiments. The matrix elements $(\chi^{QPT/PPC}_{im})_{ij}$ can be attributed to numerical errors. They are in the range of the statistical error present in the simulation and therefore do not contribute to the characterization analysis. We observed statistically relevant values for χ^{QPT}_{im} in the physical experiments and negligible values in χ^{PPA}_{im}, other consequence of the SPAM mitigation in the PPC process for one-qubit quantum processes. The PPC implements the mitigation of single qubit over-rotations, therefore the imaginary part χ^{QPT}_{im} exhibits relevant data that reflects other quantum imperfections. We establish the difference of the process matrices via the distance $d_\infty(\cdot,\cdot)$, and the process fidelity as performance metric that gives a perfect score in the noiseless simulation for the PPC (see Table I).

Additionally, the PPC protocol allows the calculation of the error process matrix directly from the quantum gate's characterization without appealing to the QPT process introduced by Korotkov [14]. The imaginary part of the error process matrix provides information about the process fidelity and imperfections. A natural extension of this work is studying the error process matrix for low-depth quantum circuits. The method may also prove useful in providing tighter measures of crosstalk effects in quantum processes. For example, tomography on one qubit, while its neighbors undergo local unitaries, can reveal correlated noise [41, 42]. The improved scalability of PPC over QPT allows us to extend this tomographic method to more significant numbers of qubits, a valuable feature for crosstalk identification and characterization.

Appendix A: Quantum process tomography implementation

The QPT algorithm finds the process matrix $\chi_\mathcal{E}$ of a quantum map $\mathcal{E} : |\rho\rangle\rangle \to |E\rho E^\dagger\rangle\rangle$, by measuring the resulting state $\mathcal{E}|\rho_k\rangle\rangle$, from a basis of initial states $\mathcal{P} : \{|\rho_1\rangle\rangle, \cdots, |\rho_{4^n}\rangle\rangle\}$, onto different directions $\mathcal{M} : \{|E_1\rangle\rangle, \cdots, |E_M\rangle\rangle\}$ in the Hilbert space, with n and M as the number of qubits and number of measurement operators respectively. Here, we have introduced the superop-

erator notation for the statistical operator, where operators become superkets and quantum maps becomes superoperators, i.e, $\mathcal{E}(\rho) \to \mathcal{E}|\rho\rangle\rangle$ (more details in [43, 44]). In the superoperator notation, the goal is to determine the matrix representation $[\chi_\mathcal{E}]_{ij} = \langle\langle j||\mathcal{E}||i\rangle\rangle$ in the Pauli basis $\{|i\rangle\rangle\}$, by the measurements

$$\lambda_{ij} = \langle\langle E_j|\mathcal{E}|\rho_i\rangle\rangle. \tag{A1}$$

We can establish the relation between λ and $\chi_\mathcal{E}$ by inserting the completeness identity $\sum_i |i\rangle\rangle\langle\langle i| = \mathbb{I}$ in Eq. A1,

$$\lambda_{ij} = \sum_{k,l=1}^{4^n} [\chi_\mathcal{E}]_{lk}\ \langle\langle E_j|k\rangle\rangle\langle\langle l|\rho_i\rangle\rangle. \tag{A2}$$

We can arrange the terms as

$$y_{j+(i-1)\times M} = \lambda_{ij}, \tag{A3}$$
$$x_{k+(l-1)\times 4^n} = [\chi_\mathcal{E}]_{ij} \tag{A4}$$
$$B_{j+(i-1)\times M,\, k+(l-1)\times 4^n} = \langle\langle E_j|k\rangle\rangle\langle\langle l|\rho_i\rangle\rangle, \tag{A5}$$

and transform A2 into a more convenient expression, $B\,\vec{x} - \vec{y} = 0$, for a numerical solution.

B.1 One-qubit process matrix: Without loss of generality, consider the characterization of a one-qubit quantum map $\mathcal{E}$ using the following intitial states and measurement operators

$$\begin{aligned}\mathcal{P} : \{\ &|Z_p\rangle\rangle, |Z_m\rangle\rangle, \\ &|X_p\rangle\rangle, |Y_p\rangle\rangle\ \}\quad ,\end{aligned} \qquad \begin{aligned}\mathcal{M} : \{\ &|Z_p\rangle\rangle, |Z_m\rangle\rangle, \\ &|X_p\rangle\rangle, |X_m\rangle\rangle, \\ &|Y_p\rangle\rangle, |Y_m\rangle\rangle\ \}\quad ,\end{aligned} \tag{A6}$$

where we have introduced the projectors $Z_p = (\mathbb{I}+\sigma_z)/2$, $Z_m = (\mathbb{I}-\sigma_z)/2$, $X_{p/m} = Y_{-\pi/2} Z_{p/m} Y_{\pi/2}$, and $Y_{p/m} = X_{-\pi/2} Z_{p/m} X_{\pi/2}$. Since $Z_p = |0\rangle\langle 0|$, $Z_m = |1\rangle\langle 1|$, $X_p = |+\rangle\langle +|$, and $Y_p = |i\rangle\langle i|$, the set $\mathcal{P}$ is generated by the preparation of the states $\{|0\rangle, |1\rangle, |+\rangle, |i\rangle\}$. The quantum chip detector measures σ_z by default. The possible outcomes of a measurement on an arbitrary state ρ are $i = 0, 1$, where $i = 0$ corresponds to $\langle\sigma_z\rangle = +1$ and $i = 1$ to $\langle\sigma_z\rangle = -1$, with probabilities

$$p_0 = \mathrm{tr}\{\rho Z_p\}, \quad p_1 = \mathrm{tr}\{\rho Z_m\}. \tag{A7}$$

Now, to measure σ_x and σ_y we need to consider the projectors X_p, X_m, and Y_p, Y_m, respectively, by transforming the x- and y-axis into the z-axis in the Bloch sphere and measuring σ_z (see the definitions below Eq. A6). Therefore, the set $\mathcal{M}$ is generated by the gates $\{\mathbb{I}, Y_{-\pi/2}, X_{-\pi/2}\}$. In Figure 5 there is a sketch of the required circuits to gate characterization. Thus, the number of quantum circuits for a complete characterization is less than the number of independent terms in the matrix process $\chi_\mathcal{E}$. On the other hand, one can observe that the number of measurement operators, size of $\mathcal{M}$, is enough for the solution of Eq. A1, since $\dim\{\mathcal{M}\} \times \dim\{\mathcal{P}\} > \dim\{\vec{y}\}$.

B.2 n-qubit process matrix: The natural extension of the initial states and the measurement operators in the n-qubit quantum process characterization follows:

$$\begin{aligned}\mathcal{P}_n : \{\ &|Z_p\rangle\rangle, |Z_m\rangle\rangle, \\ &|X_p\rangle\rangle, |Y_p\rangle\rangle\ \}^{\otimes n}\quad ,\end{aligned} \qquad \begin{aligned}\mathcal{M}_n : \{\ &|Z_p\rangle\rangle, |Z_m\rangle\rangle, \\ &|X_p\rangle\rangle, |X_m\rangle\rangle, \\ &|Y_p\rangle\rangle, |Y_m\rangle\rangle\ \}^{\otimes n}\quad ,\end{aligned} \tag{A8}$$

where $\mathcal{P}_n$ is generated by the preparation preparation of the states $\{|0\rangle, |1\rangle, |+\rangle, |i\rangle\}^{\otimes n}$. Now, the possible outcomes of the $\sigma_z^{\otimes n}$ measurement on an arbitrary state are $s = \{0, 1\}^n$, with probabilities

$$\begin{aligned} p_{0\cdots 0} &= \mathrm{tr}\{Z_p \otimes \cdots \otimes Z_p\} \\ p_{010\cdots 0} &= \mathrm{tr}\{Z_p \otimes Z_m \otimes Z_p \otimes \cdots \otimes Z_p\} \\ &\vdots \\ p_{1\cdots 1} &= \mathrm{tr}\{Z_m \otimes \cdots \otimes Z_m\}. \end{aligned} \tag{A9}$$

For the $\{\sigma_z, \sigma_y, \sigma_z\}^{\otimes n}$ measurements we need to apply the projectors $\{X_p, X_n\}^{\otimes n}$ and $\{Y_p, Y_n\}^{\otimes n}$, respectively. Thus, the set $\mathcal{M}_n$ is generated by $\{\mathbb{I}, Y_{-\pi/2}, X_{-\pi/2}\}^{\otimes n}$. Again, as in the one-qubit case, we get a redundant amount of measurements, $\dim\{\mathcal{M}_n\} \times \dim\{\mathcal{P}_n\} = 4^n \times 6^n$ for the number 16^n of independent elements in χ.

Appendix B: Fitting parameters

In this section we shall discuss the fitting details used in the post-processing step in the PPC protocol.

The number of rotations and shots plays an essential role in the quantum process characterization. We consider a one-qubit experiment to benchmark the calibration process, which follows the same principle as the characterization. In this experiment, we consider the qubit 0 in the IBMQ-Bogota quantum chip. For the calibration we use rotations about the x- and y-axis, with a different number of rotations and shots. Figure 6 shows the conditional probabilities and the initial phase for each experimental setup as a function of the number of rotations and shots, with error bars indicating the standard deviation in each measurement. We choose a suitable setup where the conditional probabilities do not vary significantly concerning the result using the highest values $N_\theta = 71$ and $N = 5000$. For Y_θ and X_θ we found the optimal points $N_\theta = 51$ and $N_\theta = 41$, respectively (see

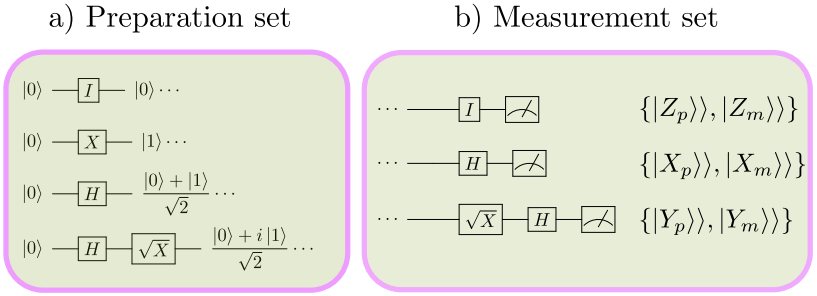

FIG. 5. Preparation and Measurement set of quantum circuits for one-qubit quantum process tomography.

shadow regions in Figure 6). One important feature is the dependence of the parameters' standard deviation on N_θ and N, which slightly improves the experimental setup's refinement.

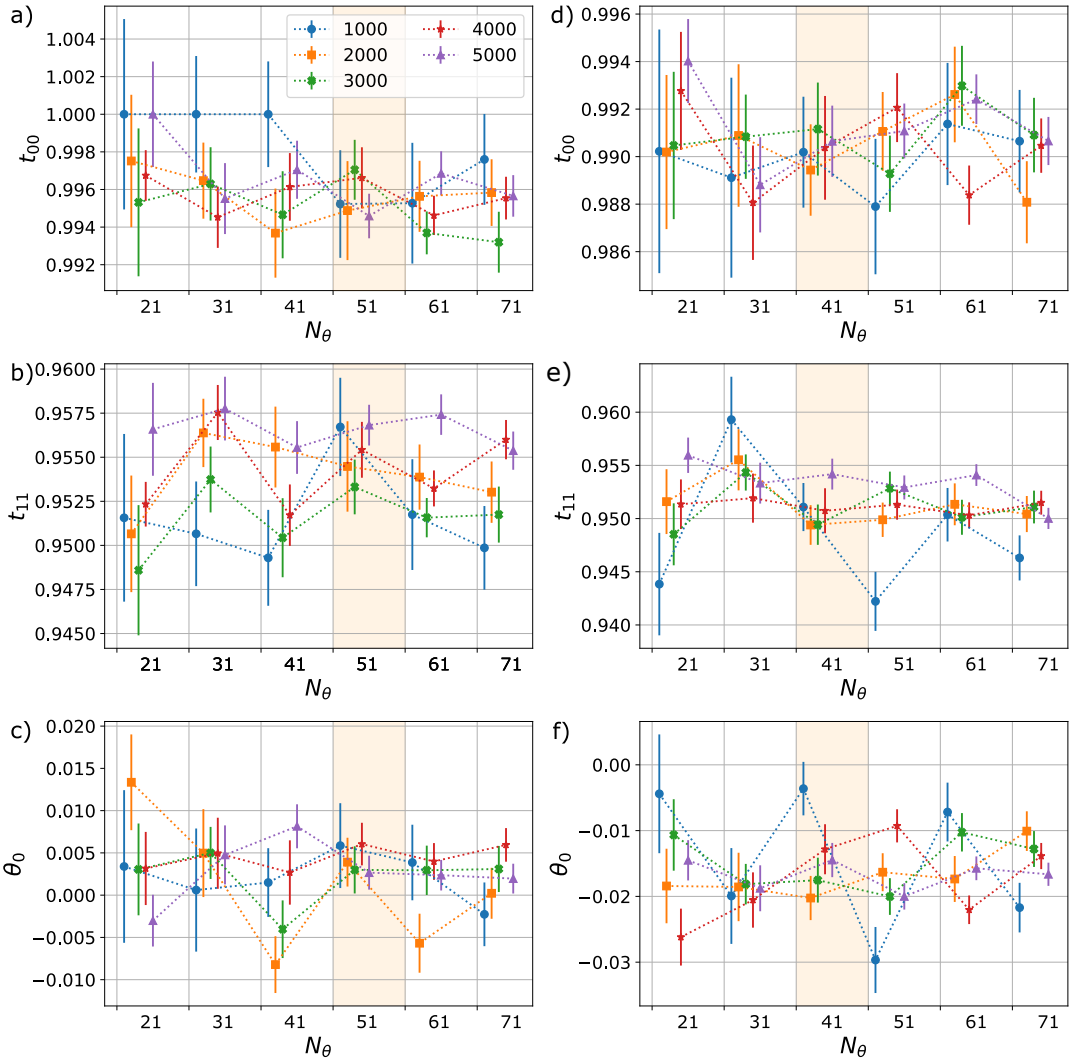

FIG. 6. *Fitting parameters:* Conditional probabilities and initial phase using Y_θ rotation in a), b), and c), and using the X_θ rotation in d), e), and f), respectively. The error bars represent the standard deviation of each parameter in the fitting process. The shadow regions indicate the optimal values for N_θ and N.

Appendix C: On-hardware experimental setup

In the Figure 7 we present the specifications of the hardware used in our experiments. The IBM hardware is subject to daily calibration, therefore, the information presented here represents an estimate, for updated values the reader can check the IBM Quantum Services [45].

IBMQ Quantum Backend Specifications

backend	topology	n_q	$\bar{\mathcal{E}}_r$	$\bar{\mathcal{E}}_{SX}$	$\bar{\mathcal{E}}_{CX}$
ibmq_bogota	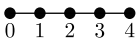	5	0.06	$4.4\text{x}10^{-4}$	$1.7\text{x}10^{-2}$
ibmq_santiago	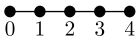	5	0.03	$3.4\text{x}10^{-4}$	$2.7\text{x}10^{-2}$
ibmq_quito	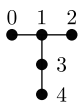	5	0.03	$4.6\text{x}10^{-4}$	$1.3\text{x}10^{-2}$
ibmq_manhattan	retired	65	0.02	$4.4\text{x}10^{-4}$	$1.3\text{x}10^{-2}$
ibmq_boeblingen	retired	20	0.05	$1.1\text{x}10^{-3}$	$1.6\text{x}10^{-2}$

FIG. 7. *Backend Specifications*: inside n_q stands for the number of qubits, $\bar{\mathcal{E}}_r$ for the average readout error rate, $\bar{\mathcal{E}}_{SX}$ for the average SX error rate, and $\bar{\mathcal{E}}_{CX}$ for the average CX error rate.

ACKNOWLEDGMENTS

We thank Ryan Bennink for valuable discussions. This work was supported as part of the ASCR Quantum Testbed Pathfinder Program at Oak Ridge National Laboratory under FWP # ERKJ332. This research used resources of the Oak Ridge Leadership Computing Facility, which is a DOE Office of Science User Facility supported under Contract DE-AC05-00OR22725.

AUTHOR CONTRIBUTIONS

V.L.O. introduced the PPC method. V.L.O. and T.K. developed the theoretical formalism, performed the analytic calculations and performed the experiments. R.C.P. analyzed and interpreted experimental data and suggested experiments to run. V.L.O, T.K., and R.C.P. cowrote the manuscript.

COMPETING INTERESTS

The authors declare that there are no competing interests.

[1] E. Magesan, J. M. Gambetta, B. R. Johnson, C. A. Ryan, J. M. Chow, S. T. Merkel, M. P. da Silva, G. A. Keefe, M. B. Rothwell, T. A. Ohki, M. B. Ketchen, and M. Steffen, Efficient measurement of quantum gate error by interleaved randomized benchmarking, Phys. Rev. Lett. **109**, 080505 (2012).

[2] J. Eisert, D. Hangleiter, N. Walk, I. Roth, D. Markham, R. Parekh, U. Chabaud, and E. Kashefi, Quantum certification and benchmarking, Nature Reviews Physics **2**, 382 (2020).

[3] M. A. Nielsenand I. L. Chuang, *Quantum Computation and Quantum Information: 10th Anniversary Edition*, 10th ed. (Cambridge University Press, USA, 2011).

[4] J. F. Poyatos, J. I. Cirac, and P. Zoller, Complete Characterization of a Quantum Process: The Two-Bit Quantum Gate, Phys. Rev. Lett. **78**, 390 (1997), arXiv:quant-ph/9611013 [quant-ph].

[5] I. L. Chuangand M. A. Nielsen, Prescription for experimental determination of the dynamics of a quantum black box, Journal of Modern Optics **44**, 2455 (1997), arXiv:quant-ph/9610001 [quant-ph].

[6] T. Baumgratz, D. Gross, M. Cramer, and M. Plenio, Scalable reconstruction of density matrices, Physical Review Letters **111**, 10.1103/PhysRevLett.111.020401 (2013).

[7] R. Blume-Kohout, Optimal, reliable estimation of quantum states, New Journal of Physics **12**, 10.1088/1367-2630/12/4/043034 (2010).

[8] C. Ferrie, Quantum model averaging, New Journal of Physics **16**, 10.1088/1367-2630/16/9/093035 (2014).

[9] R. Blume-Kohout, Robust Error Bars for Quantum Tomography (2012), cited By 30.

[10] M. Christandland R. Renner, Reliable quantum state tomography, Physical Review Letters **109**, 10.1103/PhysRevLett.109.120403 (2012).

[11] J. Wang, V. Scholz, and R. Renner, Confidence polytopes in quantum state tomography, Physical Review Letters **122**, 10.1103/PhysRevLett.122.190401 (2019).

[12] S. Zhang, Y. Lu, K. Zhang, W. Chen, Y. Li, J.-N. Zhang, and K. Kim, Error-mitigated quantum gates exceeding physical fidelities in a trapped-ion system, Nature Communications **11**, 587 (2020).

[13] T. Alexander, N. Kanazawa, D. J. Egger, L. Capelluto, C. J. Wood, A. Javadi-Abhari, and D. C. McKay, Qiskit pulse: programming quantum computers through the cloud with pulses, Quantum Science and Technology **5**, 044006 (2020).

[14] A. N. Korotkov, Error matrices in quantum process tomography (2013), arXiv:1309.6405 [quant-ph].

[15] M. Mohseni, A. T. Rezakhani, and D. A. Lidar, Quantum-process tomography: Resource analysis of different strategies, Phys. Rev. A **77**, 032322 (2008), arXiv:quant-ph/0702131 [quant-ph].

[16] G.-D. Lu, Z. Zhang, Y. Dai, Y.-L. Dong, and C.-J. Zhang, Not all entangled states are useful for ancilla-assisted quantum process tomography, Annalen der Physik , 2100550 (2022).

[17] J. B. Altepeter, D. Branning, E. Jeffrey, T. C. Wei, P. G. Kwiat, R. T. Thew, J. L. O'Brien, M. A. Nielsen, and A. G. White, Ancilla-Assisted Quantum Process Tomography, Phys. Rev. Lett. **90**, 193601 (2003), arXiv:quant-ph/0303038 [quant-ph].

[18] D. W. Leung, Chois proof as a recipe for quantum process tomography, Journal of Mathematical Physics **44**, 528 (2003), https://aip.scitation.org/doi/pdf/10.1063/1.1518554.

[19] G. M. D'Arianoand P. Lo Presti, Imprinting complete information about a quantum channel on its output state, Phys. Rev. Lett. **91**, 047902 (2003).

[20] G. M. D'Arianoand P. Lo Presti, Quantum tomography for measuring experimentally the matrix elements of an arbitrary quantum operation, Phys. Rev. Lett. **86**, 4195 (2001).

[21] S. Omkar, R. Srikanth, and S. Banerjee, Characterization of quantum dynamics using quantum error correction, Phys. Rev. A **91**, 012324 (2015).

[22] S. Omkar, R. Srikanth, and S. Banerjee, Quantum code for quantum error characterization, Phys. Rev. A **91**, 052309 (2015).

[23] M. Mohseniand D. A. Lidar, Direct characterization of quantum dynamics, Phys. Rev. Lett. **97**, 170501 (2006).

[24] M. Mohseniand D. A. Lidar, Direct characterization of quantum dynamics: General theory, Phys. Rev. A **75**, 062331 (2007).

[25] D. Gross, Y.-K. Liu, S. T. Flammia, S. Becker, and J. Eisert, Quantum state tomography via compressed sensing, Phys. Rev. Lett. **105**, 150401 (2010).

[26] S. Flammia, D. Gross, Y.-K. Liu, and J. Eisert, Quantum tomography via compressed sensing: Error bounds, sample complexity and efficient estimators, New Journal of Physics **14**, 10.1088/1367-2630/14/9/095022 (2012).

[27] A. V. Rodionov, A. Veitia, R. Barends, J. Kelly, D. Sank, J. Wenner, J. M. Martinis, R. L. Kosut, and A. N. Korotkov, Compressed sensing quantum process tomography for superconducting quantum gates, Phys. Rev. B **90**, 144504 (2014).

[28] A. Shabani, R. L. Kosut, M. Mohseni, H. Rabitz, M. A. Broome, M. P. Almeida, A. Fedrizzi, and A. G. White, Efficient Measurement of Quantum Dynamics via Compressive Sensing, Phys. Rev. Lett. **106**, 100401 (2011), arXiv:0910.5498 [quant-ph].

[29] J. Emerson, R. Alicki, and K. Zyczkowski, Scalable noise estimation with random unitary operators, Journal of Optics B: Quantum and Semiclassical Optics **7**, S347 (2005).

[30] E. Knill, D. Leibfried, R. Reichle, J. Britton, R. B. Blakestad, J. D. Jost, C. Langer, R. Ozeri, S. Seidelin, and D. J. Wineland, Randomized benchmarking of quantum gates, Phys. Rev. A **77**, 012307 (2008), arXiv:0707.0963 [quant-ph].

[31] E. Magesan, J. Gambetta, and J. Emerson, Scalable and robust randomized benchmarking of quantum processes, Physical Review Letters **106**, 10.1103/PhysRevLett.106.180504 (2011).

[32] L. C. G. Govia, G. J. Ribeill, D. Ristè, M. Ware, and H. Krovi, Bootstrapping quantum process tomography via a perturbative ansatz, Nature Communications **11**, 10.1038/s41467-020-14873-1 (2020).

[33] D. Ahn, Y. S. Teo, H. Jeong, F. Bouchard, F. Hufnagel, E. Karimi, D. Koutný, J. Řeháček, Z. Hradil, G. Leuchs, and L. L. Sánchez-Soto, Adaptive compressive tomography with no a priori information, Phys. Rev. Lett. **122**, 100404 (2019).

[34] D. Ahn, Y. S. Teo, H. Jeong, D. Koutný, J. Řeháček, Z. Hradil, G. Leuchs, and L. L. Sánchez-Soto, Adaptive compressive tomography: A numerical study, Phys. Rev. A **100**, 012346 (2019).

[35] Y. Kim, Y. S. Teo, D. Ahn, D.-G. Im, Y.-W. Cho, G. Leuchs, L. L. Sánchez-Soto, H. Jeong, and Y.-H. Kim, Universal compressive characterization of quantum dynamics, Phys. Rev. Lett. **124**, 210401 (2020).

[36] Y. S. Teo, G. I. Struchalin, E. V. Kovlakov, D. Ahn, H. Jeong, S. S. Straupe, S. P. Kulik, G. Leuchs, and L. L. Sánchez-Soto, Objective compressive quantum process tomography, Phys. Rev. A **101**, 022334 (2020).

[37] R. Martinand K. Peter, symfit (2020).

[38] H. Abraham, AduOffei, R. Agarwal, I. Y. Akhalwaya, G. Aleksandrowicz, T. Alexander, M. Amy, E. Arbel, Arijit02, A. Asfaw, A. Avkhadiev, C. Azaustre, AzizNgoueya, A. Banerjee, A. Bansal, P. Barkoutsos, A. Barnawal, G. Barron, G. S. Barron, L. Bello, Y. Ben-Haim, D. Bevenius, A. Bhobe, L. S. Bishop, C. Blank, S. Bolos, S. Bosch, Brandon, S. Bravyi, Bryce-Fuller, D. Bucher, A. Burov, F. Cabrera, P. Calpin, L. Capelluto, J. Carballo, G. Carrascal, A. Chen, C.-F. Chen, E. Chen, J. C. Chen, R. Chen, J. M. Chow, S. Churchill, C. Claus, C. Clauss, R. Cocking, F. Correa, A. J. Cross, A. W. Cross, S. Cross, J. Cruz-Benito, C. Culver, A. D. Córcoles-Gonzales, S. Dague, T. E. Dandachi, M. Daniels, M. Dartiailh, DavideFrr, A. R. Davila, A. Dekusar, D. Ding, J. Doi, E. Drechsler, Drew, E. Dumitrescu, K. Dumon, I. Duran, K. EL-Safty, E. Eastman, G. Eberle, P. Eendebak, D. Egger, M. Everitt, P. M. Fernández, A. H. Ferrera, R. Fouilland, FranckChevallier, A. Frisch, A. Fuhrer, B. Fuller, M. GEORGE, J. Gacon, B. G. Gago, C. Gambella, J. M. Gambetta, A. Gammanpila, L. Garcia, T. Garg, S. Garion, A. Gilliam, A. Giridharan, J. Gomez-Mosquera, Gonzalo, S. de la Puente González, J. Gorzinski, I. Gould, D. Greenberg, D. Grinko, W. Guan, J. A. Gunnels, M. Haglund, I. Haide, I. Hamamura, O. C. Hamido, F. Harkins, V. Havlicek, J. Hellmers, Ł. Herok, S. Hillmich, H. Horii, C. Howington, S. Hu, W. Hu, J. Huang, R. Huisman, H. Imai, T. Imamichi, K. Ishizaki, R. Iten, T. Itoko, JamesSeaward, A. Javadi, A. Javadi-Abhari, W. Javed, Jessica, M. Jivrajani, K. Johns, S. Johnstun, JonathanShoemaker, V. K, T. Kachmann, A. Kale, N. Kanazawa, Kang-Bae, A. Karazeev, P. Kassebaum, J. Kelso, S. King, Knabberjoe, Y. Kobayashi, A. Kovyrshin, R. Krishnakumar, V. Krishnan, K. Krsulich, P. Kumkar, G. Kus, R. LaRose, E. Lacal, R. Lambert, J. Lapeyre, J. Latone, S. Lawrence, C. Lee, G. Li, D. Liu, P. Liu, Y. Maeng, K. Majmudar, A. Malyshev, J. Manela, J. Marecek, M. Marques, D. Maslov, D. Mathews, A. Matsuo, D. T. McClure, C. McGarry, D. McKay, D. McPherson, S. Meesala, T. Metcalfe, M. Mevissen, A. Meyer, A. Mezzacapo, R. Midha, Z. Minev, A. Mitchell, N. Moll, J. Montanez, G. Monteiro, M. D. Mooring, R. Morales, N. Moran, M. Motta, MrF, P. Murali, J. Müggenburg, D. Nadlinger, K. Nakanishi, G. Nannicini, P. Nation, E. Navarro, Y. Naveh, S. W. Neagle, P. Neuweiler, J. Nicander, P. Niroula, H. Norlen, NuoWenLei, L. J. O'Riordan, O. Ogunbayo, P. Ollitrault, R. Otaolea, S. Oud, D. Padilha, H. Paik, S. Pal, Y. Pang, V. R. Pascuzzi, S. Perriello, A. Phan, F. Piro, M. Pistoia,

C. Piveteau, P. Pocreau, A. Pozas-iKerstjens, M. Prokop, V. Prutyanov, D. Puzzuoli, J. Pérez, Quintiii, R. I. Rahman, A. Raja, N. Ramagiri, A. Rao, R. Raymond, R. M.-C. Redondo, M. Reuter, J. Rice, M. Riedemann, M. L. Rocca, D. M. Rodríguez, RohithKarur, M. Rossmannek, M. Ryu, T. SAPV, SamFerracin, M. Sandberg, H. Sandesara, R. Sapra, H. Sargsyan, A. Sarkar, N. Sathaye, B. Schmitt, C. Schnabel, Z. Schoenfeld, T. L. Scholten, E. Schoute, J. Schwarm, I. F. Sertage, K. Setia, N. Shammah, Y. Shi, A. Silva, A. Simonetto, N. Singstock, Y. Siraichi, I. Sitdikov, S. Sivarajah, M. B. Sletfjerding, J. A. Smolin, M. Soeken, I. O. Sokolov, I. Sokolov, SooluThomas, Starfish, D. Steenken, M. Stypulkoski, S. Sun, K. J. Sung, H. Takahashi, T. Takawale, I. Tavernelli, C. Taylor, P. Taylour, S. Thomas, M. Tillet, M. Tod, M. Tomasik, E. de la Torre, K. Trabing, M. Treinish, TrishaPe, D. Tulsi, W. Turner, Y. Vaknin, C. R. Valcarce, F. Varchon, A. C. Vazquez, V. Villar, D. Vogt-Lee, C. Vuillot, J. Weaver, J. Weidenfeller, R. Wieczorek, J. A. Wildstrom, E. Winston, J. J. Woehr, S. Woerner, R. Woo, C. J. Wood, R. Wood, S. Wood, S. Wood, J. Wootton, D. Yeralin, D. Yonge-Mallo, R. Young, J. Yu, C. Zachow, L. Zdanski, H. Zhang, C. Zoufal, Zoufalc, a kapila, a matsuo, bcamorrison, brandhsn, nick bronn, brosand, chlorophyll zz, csseifms, dekel.meirom, dekelmeirom, dekool, dime10, drholmie, dtrenev, ehchen, elfrocampeador, faisaldebouni, fanizzamarco, gabrieleagl, gadial, galeinston, georgios ts, gruu, hhorii, hykavitha, jagunther, jliu45, jscott2, kanejess, klinvill, krutik2966, kurarrr, lerongil, ma5x, merav aharoni, michelle4654, ordmoj, sagar pahwa, rmoyard, saswati qiskit, scottkelso, sethmerkel, shaashwat, sternparky, strickroman, sumitpuri, tigerjack, toural, tsura crisaldo, vvilpas, welien, willhbang, yang.luh, yotamvakninibm, and M. Čepulkovskis, Qiskit: An open-source framework for quantum computing (2019), accessed: 12-11-2020.

[39] L. Knips, C. Schwemmer, N. Klein, J. Reuter, G. Tóth, and H. Weinfurter, How long does it take to obtain a physical density matrix?, arXiv preprint arXiv:1512.06866 (2015).

[40] P. Gokhale, A. Javadi-Abhari, N. Earnest, Y. Shi, and F. T. Chong, Optimized quantum compilation for near-term algorithms with openpulse, in *2020 53rd Annual IEEE/ACM International Symposium on Microarchitecture (MICRO)* (IEEE, 2020) pp. 186–200.

[41] R. Blume-Kohout, E. Nielsen, K. Rudinger, K. Young, M. Sarovar, and T. Proctor, Idle tomography: Efficient gate characterization for n-qubit processors, in *APS March Meeting Abstracts*, Vol. 2019 (2019) pp. P35–006.

[42] A. Ash-Saki, M. Alam, and S. Ghosh, Experimental characterization, modeling, and analysis of crosstalk in a quantum computer, IEEE Transactions on Quantum Engineering **1**, 1 (2020).

[43] D. Greenbaum, Introduction to quantum gate set tomography, arXiv preprint arXiv:1509.02921 (2015).

[44] E. Nielsen, J. K. Gamble, K. Rudinger, T. Scholten, K. Young, and R. Blume-Kohout, Gate set tomography, Quantum **5**, 557 (2021).

[45] IBM-Quantum, https://quantum-computing.ibm.com/ (2021).